Progress In Electromagnetics Research, Vol. 175, 1–11, 2022

Machine-Learning-Enabled Recovery of Prior Information from Experimental Breast Microwave Imaging Data

Keeley Edwards, Joe LoVetri, Colin Gilmore, and Ian Jeffrey

Abstract—We demonstrate the recovery of simple geometric and permittivity information of breast models in an experimental microwave breast imaging system using a synthetically trained machine learning workflow. The recovered information consists of simple models of adipose and fibroglandular regions. The machine learning model is trained on a labelled synthetic dataset constructed over a range of possible adipose and fibroglandular regions and the trained neural network predicts the geometry and average permittivty of the adipose and fibroglandular regions from calibrated experimental data. The proposed workflow is tested on two different experimental models of the human breast. The first model is comprised of two simple, symmetric phantoms representing the adipose and fibroglandular regions of the breast that match the model used to train the neural network. The second, more realistic model replaces the symmetric fibroglandular phantom with an irregularly shaped, MRI-derived fibroglandular phantom. We demonstrate the ability of the machine learning workflow to accurately recover geometry and complex valued average permittivity of the fibroglandular region for the simple case, and to predict a symmetric convex hull that is a reasonable approximation to the proportions of the MRI-derived fibroglandular phantom.

1. INTRODUCTION

Microwave imaging of the human breast continues to be investigated as a technology that may be used for the detection of breast cancer and for monitoring tumor response to treatment. Ongoing research in the inverse scattering and microwave imaging communities has shown that the reconstruction of models of the human breast can provide information on the structure and material properties of breast tissue both synthetically and experimentally [1, 2]. Microwave imaging technologies do not generate high resolution images like those obtained from x-ray or computed tomography (CT), but by using microwaves rather than x-rays, the technology is beneficial as it relies on non-ionizing radiation and may have utility as a lower-cost screening tool [3]. An effective screening tool would provide information to characterize different tissue regions within the breast based on location, geometry, and physical properties of the tissue. In the case of electromagnetic imaging, the complex-valued permittivity, ε, of the tissue is of interest, as different tissue types (adipose, fibroglandular, and tumor) can be differentiated by their permittivities at microwave frequencies [4].

Historically, inversion of the data collected using a microwave imaging system has been accomplished using iterative optimization algorithms such as the Contrast Source Inversion method (CSI) [5, 6] or Gauss Newton Inversion [7–9]. Having accurate prior information about the region of interest can greatly improve the quality of reconstructions obtained using such inversion algorithms [10–13]. In the case of CSI, this prior information serves as the background for full-phase inversion, reducing the non-linearity of the inverse problem and improving the quality of the result [12, 14].

Received 16 May 2022, Accepted 16 June 2022, Scheduled 14 July 2022

* Corresponding author: Keeley Edwards (umedwa45@myumanitoba.ca).

The authors are with the Department of Electrical and Computer Engineering, Price Faculty of Engineering, University of Manitoba, Canada.

In recent years, significant attention has been paid to applying machine learning for enabling, assisting, and improving electromagnetic imaging. Machine learning approaches include obtaining prior information from the data [15], improving conventional microwave imaging results with neural networks [16–18], and data-to-image reconstructions with assumed prior information [19]. In cases where the output of the machine learning model is an image, most experimental results are 2D, and benefit from initial early iterations of imaging algorithms [17, 20]. 3D inversion results are discussed in [21, 18, 19]. Regardless of the method of inversion (iterative optimization or machine learning), acquiring the prior information in some form is a beneficial step for successful image reconstruction. It is also possible to consider the addition of accurate prior information about the target as a way of reaching the correct Riemann sheet for the phase of the recovered scattered field [9]. However it is viewed, the addition of this information improves the inversion results. This benefit is not limited to biomedical applications [22] but extends to other application areas including agricultural [23], remote sensing [24], and geophysical imaging [25], where machine learning has also been widely applied [16, 26, 27]. While the present work focuses specifically on machine learning applied to our microwave breast imaging system [2, 28], the reader is referred to [29–31] for additional review material covering a wider range of applications.

Our recent efforts have been focused on exploring the various potential applications of machine learning for 3D image reconstruction of data from electromagnetic imaging systems. We have applied these techniques to both stored grain monitoring [15, 19], and microwave breast imaging [32, 33] and have demonstrated that machine-learning-assisted parametric inversion can be an efficient way to obtain prior information about the region of interest. This approach has been successfully used to calibrate experimental data to a computational model for full phase inversion.

In this paper we focus on extracting parametric prior information from relatively simple 3D experimental breast phantoms using a fully connected neural network, but consider the specific case where the physical tissues do not match our simple model well. This work is an extension of [33] which focused primarily on synthetic tests. Here we expand upon previous synthetic tests by performing parametric inversion on synthetic data where the geometry of the phantom is not modeled by the synthetic training data. We use a synthetically trained neural network to perform a phaseless parametric inversion on calibrated experimental data that predicts a set of parameters describing the fibroglandular region of the breast.

2. THE EXPERIMENTAL BREAST MICROWAVE IMAGING SYSTEM

The experimental system adopted for this work, shown in Figure 1, is a faceted, 24-transceiver imaging system designed for tumor monitoring and detection in the human breast [28]. The chamber has metal walls (facets) with an open-air top, creating a quasi-resonant, air-filled chamber for imaging. The transceivers (magnetic field probes), are arranged along the interior of the chamber walls, perpendicular to the flat surface of the facets. The opening at the top of the chamber is 22 cm in diameter, and we assume that the position of the breast can be fixed within the chamber to a known location prior to imaging.

2.1. Experimental Breast Model

In this work we consider two different models of the human breast. The first model, the simpler of the two, consists of two 3D-printed symmetric cups, one larger cup to represent the adipose tissue and a second smaller cup to represent the fibroglandular tissue. The smaller cup is placed within the larger cup inside the chamber, shown in Figure 2. When taking a measurement, the larger cup is filled with canola oil ($\varepsilon = 3 - 0.6j$) to represent an approximate value of the permittivity of adipose tissue over the range of frequencies measured [18], while the smaller cup is filled with a mixture of water and glycerin with a measured permittivity of $\varepsilon = 20 - 12j$ representing fibroglandular tissue. The second model is a 3D-printed realistic geometry fibroglandular phantom that was created from MRI data [34]. This MRI-derived fibroglandular phantom can be placed inside the large symmetric cup in place of the smaller symmetric cup for data collection. These breast models are simplified representations of the human breast, but are suitable for evaluating parametric prior information recovery.

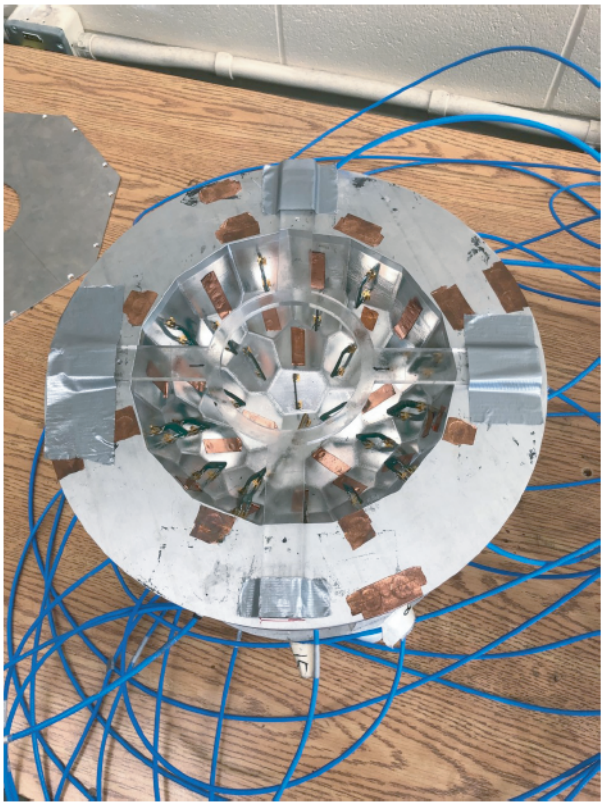

Figure 1. Empty faceted chamber with an open-top and a clear plastic holder used to fix the position of the phantoms.

2.2. Experimental Data Collection

During experimental measurements, the fluid-filled breast phantoms are placed within the faceted chamber at a known, fixed position in the center of the chamber. The phantoms are held in place with a clear plastic holder, which is omitted from synthetic models of the system for simplicity. The experimental data is collected with the top of the chamber open to the air, the consequence of this is that unlike in a clinical setting, there is no boundary equivalent to the chest wall of the patient. To align with the experimental setup, the computational model of the system is designed such that the top of the chamber is open, as described in Section 3.1.

The field probes are designed to measure the ϕ-component of the magnetic fields, H_ϕ, tangent to the chamber wall [28] and are connected to a vector network analyzer (VNA) through coaxial cables. A 24-port VNA was used to collect the experimental data used in this work. Measurements consist of the data from each transmitter, $i = 1 \dots 24$, measured at each receiver, $j = 1 \dots 24$, at a single frequency, resulting in a 24×24 matrix of S-parameters which we refer to as an S-matrix.

3. SYSTEM MODEL AND CALIBRATION

3.1. Synthetic Model

Complementary to the experimental system, a synthetic model of the setup is created, such that computational forward solvers can be used to generate synthetic data representative of the faceted chamber with the model of the human breast [35, 36]. This synthetic model represents the chamber walls as a perfect electric conductor (PEC), and models a dome top above the chamber opening with an absorbing boundary condition. To reduce the size of the computations for the forward problem, the dome top is placed in relatively close proximity to the chamber opening (Figure 3), which may reduce

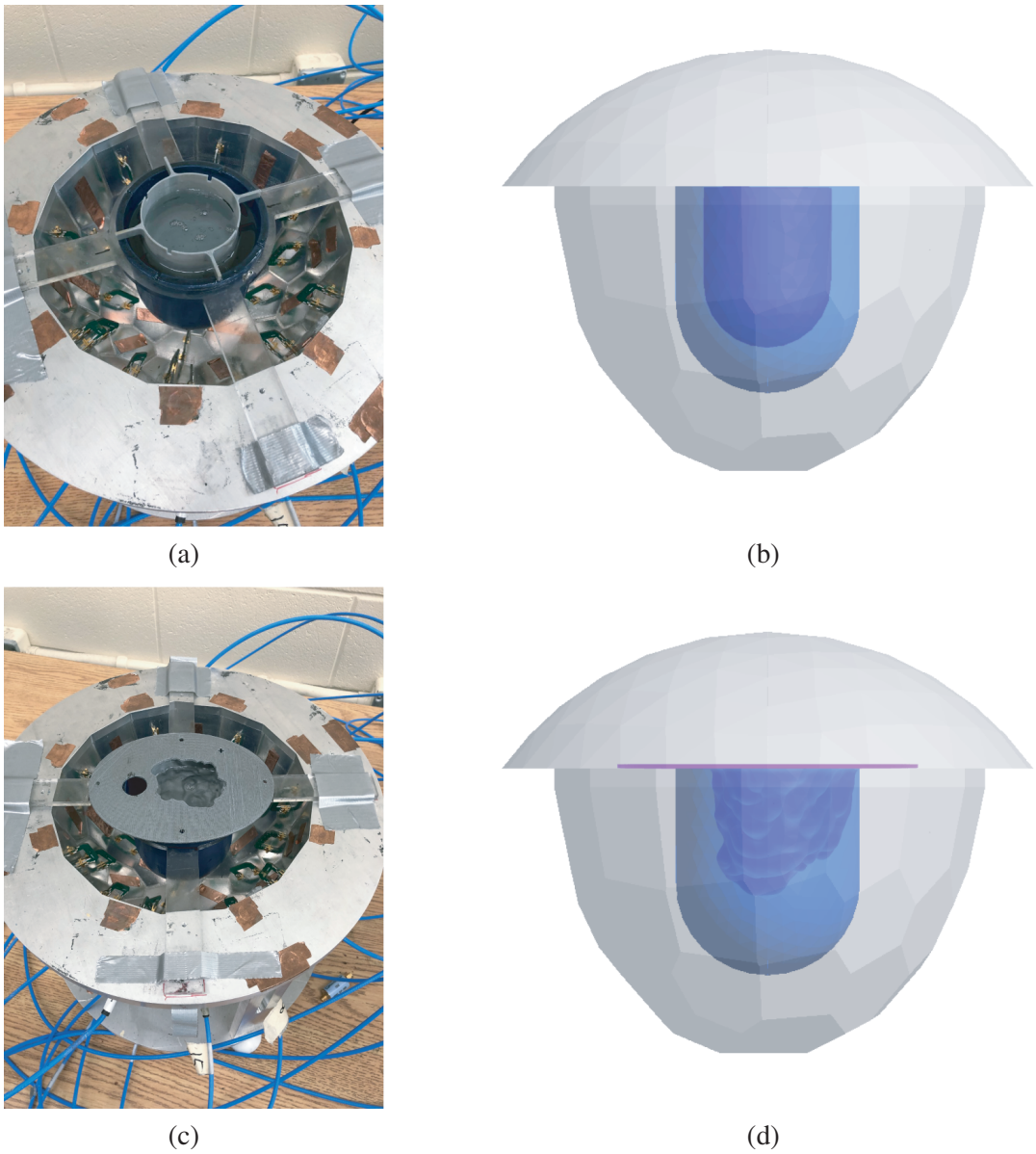

(a) (b)

(c) (d)

Figure 2. Top row: (a) Photo of the experimental setup and (b) computational render of the chamber with symmetric fibroglandular phantom. Bottom row: (c) Photo of the experimental setup and (d) computational render of the chamber with the 3D-printed MRI-derived fibroglandular phantom. The larger blue symmetric region in both photos and renders represents adipose tissue, and the smaller grey (photos) and purple (renders) regions represent fibroglandular tissue.

the accuracy of the simulation. As with the experimental setup, the breast phantoms are centered in the chamber in the synthetic model.

A Discontinuous Galerkin Method forward solver [36] was used to generate the synthetic data based on the model of the experimental setup. The chamber transceivers are modeled as point sources, centered on the corresponding flat facet, 7 mm above the inner face. As noted previously, the synthetic model of the system omits the clear plastic holder, as well as switch and cable losses, which are accounted for during calibration of the experimental data to the synthetic model.

We define the synthetic data equivalent of the experimental S-matrix as the H-matrix. Each element in the H-matrix represents the ϕ-component of the model magnetic field intensity corresponding

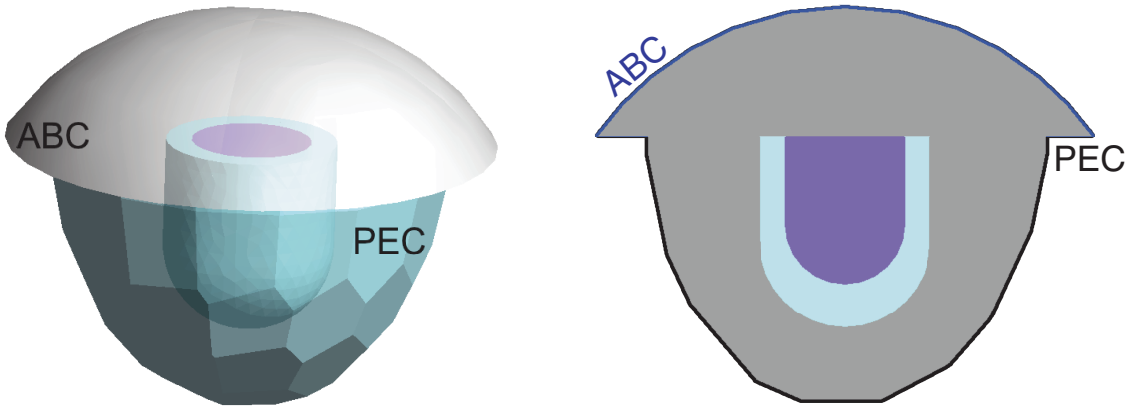

(a) (b)

Figure 3. (a) 3D model of the experimental system, with symmetric adipose (light blue) and fibroglandular (purple) phantoms. The PEC surface of the faceted chamber is shown in blue, and the open-top dome shaped absorbing boundary (ABC) surface is shown in grey. (b) A 2D slice of the model, showing the air filled region (grey), bounded by the absorbing boundary (blue) and the PEC boundary (black).

to each transmitter-receiver pair. Converting measured S-parameters to model-compatible magnetic field measurements is accomplished through calibration. During parametric inversion, we choose to omit the back-scattering measurements (S_{ii} or H_{ii}), for an overall data vector of length 552 (24×23).

3.2. Calibration

While we have previously demonstrated the ability to apply a phaseless parametric inversion workflow to uncalibrated experimental data in uncooperative systems (i.e., where traditional calibration using a known target is not possible) such as for stored grain monitoring [15], experience has shown that calibration is beneficial when evaluating data from the experimental breast microwave imaging system. The experimental breast system is cooperative in the sense that it is easy to introduce a calibration target. In this work we have chosen the calibration target as a homogeneous adipose background. Experimentally, this is achieved by placing the large symmetric (blue) 3D-printed breast phantom in the chamber and filling it with our model adipose fluid (canola oil). Synthetically, the permittivity of the entire breast tissue within the model is set to that of the model adipose fluid. We then perform an incident field calibration of the data according to:

$$H_{ij,target} = \frac{H_{ij,adipose}}{S_{ij,adipose}}(S_{ij,target} - S_{ij,adipose}) \tag{1}$$

where H_{target} are the calibrated experimental scattered fields; $H_{adipose}$ and $S_{adipose}$ are the synthetic and raw experimental fields of the adipose-only model, respectively; and S_{target} are the raw experimental fields of the adipose tissue and the target. The target is the phantom representing the fibroglandular tissue in the model of the breast.

4. THE PARAMETER SET

When attempting to solve the inverse scattering problem, it is generally beneficial to choose the background medium for the scattered field problem to incorporate as much knowledge of the target as possible. Considering the case of tumor detection/monitoring in the human breast, we are concerned with recovering the tumor as a high-contrast target embedded within the breast tissue. To accomplish this, we aim to to determine a small set of general properties of the fibroglandular tissues of the breast, within an assumed known adipose region. The experimental system design presented in Section 2 is such that the location of the breast within the chamber, as well as the boundary of the breast can

be fixed within a holder. It remains to recover knowledge of the fibroglandular region. We limit this recovery to a simple geometry and the average complex-valued permittivity of the fibroglandular tissues. This leads to a set of four parameters, $\underline{\mathbf{p}}_4$, that consists of the radius (r), height (h), and the average complex-valued permittivity ($\varepsilon = \varepsilon' + j\varepsilon''$) of the fibroglandular region. That is to say, $\underline{\mathbf{p}}_4 = [r, h, \varepsilon', \varepsilon'']$.

It should be noted that, by design, this parameter set does not allow for the reconstruction of tumor-like targets with the hopes that the recovered parameters will largely represent the average adipose and fibroglandular tissues, even if a tumor is present within the breast. Choosing the background for any subsequent inversion problem to be the adipose and fibroglandular regions of the breast (assuming they are known accurately), reduces the overall contrast and simplifies the inverse scattering problem when attempting to detect and/or monitor tumors.

5. MACHINE LEARNING ENABLED PARAMETRIC INVERSION

Full details on the neural network and the overall proposed workflow are presented in our previous work [33], but are summarized here for convenience.

5.1. Machine Learning Model

To obtain $\underline{\mathbf{p}}_4$ from experimental data, a 4-hidden-layer, fully-connected neural network accepts phaseless, calibrated S-parameter data in the form of 552 point data vector, $\underline{\mathbf{d}}$, and produces a four parameter estimate of the fibroglandular region (Figure 4). The network is trained on 4621 examples, with a batch size of 1000 for a maximum of 100 epochs, and using a residual sum of squares loss function.

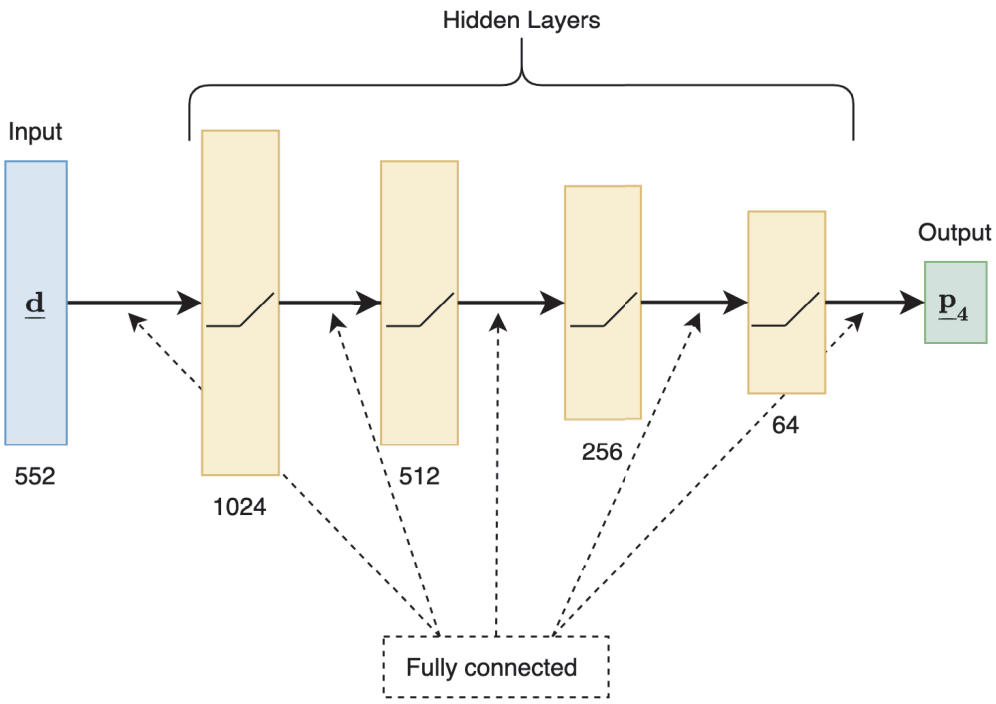

Figure 4. The 4-hidden-layer fully connected neural network. The number of neurons in each layer is given by the number below the layer. The 552-element input layer is shown in blue, hidden layers (with ReLU activation) are shown in yellow, and the 4-parameter output layer is shown in green. Horizontal arrows denote full connectivity between network layers.

5.2. Synthetic Training Data

The synthetic model described in Section 3.1 is used to generate the training set for machine learning. Each of the $\underline{\mathbf{p}}_4$ parameters is varied to construct a training set of synthetic data that represents a variety of different breast densities based on the fixed adipose size of the breast phantom, with a height of 10.9 cm and a radius of 4.8 cm, and to cover a range of fibroglandular tissue permittivities. The complete labelled dataset consists of 18,122 synthetic examples, covering the range of geometry (height and radius) and complex-valued permittivity ($\varepsilon = \varepsilon' + j\varepsilon''$) parameters for the fibroglandular tissue which are given in Table 1.

Table 1. Parameter ranges comprising the synthetic training set.

Parameter	**Minimum**	**Maximum**
Radius [cm]	2.8	4.1
Height [cm]	5.3	9.8
ε'	5.0	25.0
ε''	-25.0	-5.0

A small subset of the total labeled dataset is used for training. 30% of the dataset is randomly selected at training time, and partitioned 85%, 10%, and 5% into training, validation, and test data, respectively. As a result, the network is trained on 4621 examples.

6. RESULTS

In [33] we showed the ability of this network architecture to accurately predict $\underline{\mathbf{p}}_4$ (permittivity and geometry) of symmetric fibroglandular regions (Figure 3) from noisy synthetic data, and showed that the combination of adipose and fibroglandular tissues can be used as an appropriate background for tumor detection. In our previous attempts to recover the same parameters from calibrated experimental data for the same symmetric fibroglandular phantom used in this work we were able to accurately recover geometry information, but struggled to recover reasonable estimates for the permittivity of the fibroglandular tissue.

6.1. Experimental Symmetric Fibroglandular Region

Here, we demonstrate successful recovery of $\underline{\mathbf{p}}_4$ from calibrated experimental data. Two recent changes made to the parametric inversion process are 1) a 25% reduction in the size of the training set and 2) an expansion of the parameter ranges for the bulk complex-valued permittivity in the training set. In [33] our preliminary tests with experimental data produced permittivity predictions that were near the boundary or outside of the range of permittivities used within the training set. The errors in these predictions led us to increase the range of permittivities used for training the neural network used in this work. Following these changes we are able to maintain height and radius predictions that are accurate to within 2 mm, while reducing the error in the real part of the permittivity to within 2.0 and the complex valued permittivity to within 0.5 (Table 2), where previously the predicted errors were as large as 8.4 and 7.4, for real and imaginary permittivities, respectively [33].

Table 2. Predictions for the symmetric fibroglandular region experimental data.

Example	**Radius [cm]**	**Height [cm]**	ε'	ε''
True	3.4	8.5	20.0	-12.0
Measurement 1	3.5	8.6	20.1	-12.4
Measurement 2	3.4	8.6	22.0	-12.1

6.2. Synthetic Asymmetric and Off-Center Fibroglandular Region

In addition to the two experimental breast phantoms analyzed, two synthetic examples were evaluated to assess the performance of the neural network for fibroglandular regions not represented by the training set. The training set assumes fibroglandular regions are symmetric and centered, as shown in Figure 3. Synthetic measurement data was generated for an off-center fibroglandular region, as well as for an off-center and asymmetric fibroglandular region (Figure 5).

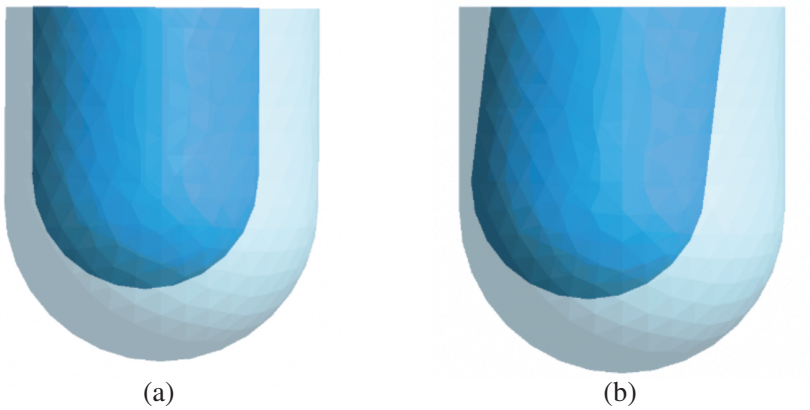

Figure 5. (a) Off-center fibroglandular phantom relative to the adipose region and (b) asymmetric and off-center fibroglandular phantom relative relative to the adipose region. Fibroglandular phantoms are shown in dark blue, with adipose regions superimposed in light blue.

Parameter predictions for these two synthetic examples are given in Table 3. The network is able to accurately recover the geometry of the fibroglandular region to within 1 mm for radius and 3 mm for height. The permittivity predictions obtained are reasonable, but not as accurate as for the centered, symmetric experimental examples given in Section 6.1; the permittivity values for the symmetric, off-center fibroglandular region are better than those for the asymmetric, off-center region, as expected.

Table 3. Predictions for the asymmetric and off-center fibroglandular region synthetic data.

Example	**Radius [cm]**	**Height [cm]**	ε'	ε''
True	3.5	8.6	20.0	−12.0
Symmetric, off-center	3.5	8.5	21.3	−11.3
Asymmetric, off-center	3.6	8.3	23.5	−8.0

6.3. Experimental MRI Derived Fibroglandular Region

To expand on the practical use of this synthetically trained neural network, we evaluate the ability to predict the convex hull geometry of an asymmetric fibroglandular region with an irregular (both convex and concave) surface. Specifically, a 3D-printed phantom of a fibroglandular region obtained from MRI data [34] was used in place of the symmetric fibroglandular phantom. Figures 2(c) and (d) show the experimental system and its computational model with the MRI derived fibroglandular region within the symmetric adipose phantom.

The results in Table 4 suggest that the neural network is able to detect the convex hull geometry of an asymmetric fibroglandular region, but struggles to accurately estimate the average complex-valued permittivity of the tissue. While focusing on the geometry predictions, upon initial inspection it appears that the radius prediction for the fibroglandular region is unacceptably low, however it is important to consider that the neural network was trained on a set of radially symmetric, smooth fibroglandular

Table 4. Predictions for the MRI-derived fibroglandular region experimental data.

Example	**Radius [cm]**	**Height [cm]**	ε'	ε''
True	3.9	7.2	20.0	−12.0
Measurement 1	3.0	6.9	10.9	−15.2
Measurement 2	2.9	6.9	10.7	−15.1

tissues, and the MRI-derived fibroglandular region is irregular, not radially symmetric, and does not have a consistent radius along its height. While we have chosen one measurement from the approximate center axis to an outer surface of this phantom as the "true" radius, there is no guarantee that the neural network is predicting this same distance. For these reasons, it is difficult to quantitatively assess the accuracy of $\underline{\mathbf{p}}_4$ and it is thus helpful to visualize the superposition of the predicted symmetric convex hull on the MRI-derived fibroglandular region to qualitatively assess the performance of the neural network. Figure 6 shows the predicted convex hull superimposed on the MRI-derived fibroglandular region, depicting how the predicted radius and height of the convex hull fits the MRI-derived phantom. While it is clear that the permittivity predictions for this phantom do not line up with the measured value for the experimental fluid, this is not completely unexpected. We speculate that the network may be predicting permittivity values that compensate for structural features that were not part of the training set such as the asymmetry and irregular surface profile of the phantom.

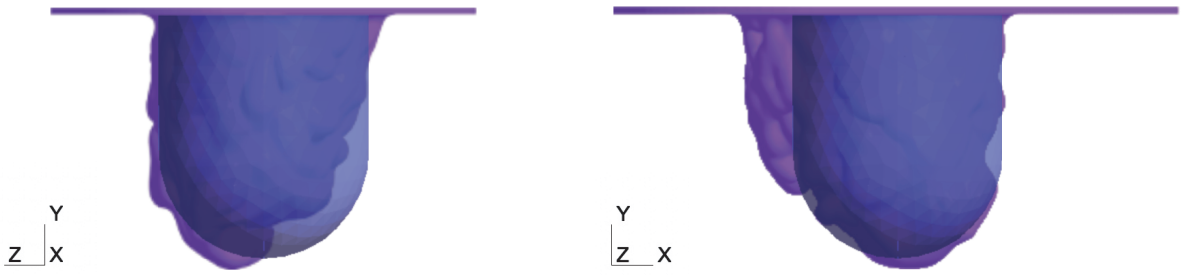

Figure 6. Predicted convex hull overlaid against the asymmetric MRI-derived fibroglandular region viewed from the (a) x-direction and (b) z-direction.

Although this realistic fibroglandular region cannot be accurately represented by only two geometry parameters, the ability to predict a convex hull which approximates the overall proportion and size of the region is valuable as prior information for eventual full inversion of data collected with this measurement system.

7. CONCLUSION

In this work we have demonstrated the ability for a synthetically trained neural network to perform parametric inversion on experimental data to recover prior information, in the form of geometry and average complex-valued permittivity, characterizing the fibroglandular tissue within a simple model of the human breast. In addition to accurately recovering both geometry and permittivity information from a symmetric fibroglandular phantom, we showed that the neural network can reasonably predict the convex hull geometry of a realistic, MRI-derived fibroglandular phantom. The ability to recover a reasonable estimate of the symmetric convex hull approximating an irregularly shaped fibroglandular phantom is significant in spite of the ongoing challenges in recovering the permittivity of this region. Research is ongoing to determine whether accurately predicted geometry alongside literature values for the permittivity of fibroglandular tissue is sufficient prior information for full inversion.

REFERENCES

1. Shea, J. D., P. Kosmas, S. C. Hagness, and B. D. Van Veen, "Three-dimensional microwave imaging of realistic numerical breast phantoms via a multiple-frequency inverse scattering technique," *Medical Physics (Lancaster)*, Vol. 37, No. 8, 4210–4226, 2010.
2. Asefi, M., A. Baran, and J. LoVetri, "An experimental phantom study for air-based quasi-resonant microwave breast imaging," *IEEE Transactions on Microwave Theory and Techniques*, Vol. 67, No. 9, 3946–3954, 2019.
3. AlSawaftah, N., S. El-Abed, S. Dhou, and A. Zakaria, "Microwave imaging for early breast cancer detection: Current state, challenges, and future directions," *Journal of Imaging*, Vol. 8, No. 5, 2022, [Online], Available: https://www.mdpi.com/2313-433X/8/5/123.
4. Lazebnik, M., D. Popovic, L. McCartney, C. B. Watkins, M. J. Lindstrom, J. Harter, S. Sewall, T. Ogilvie, A. Magliocco, T. M. Breslin, et al., "A large-scale study of the ultrawideband microwave dielectric properties of normal, benign and malignant breast tissues obtained from cancer surgeries," *Physics in Medicine & Biology*, Vol. 52, No. 20, 6093, 2007.
5. Van Den Berg, P. M. and R. E. Kleinman, "A contrast source inversion method," *Inverse Problems*, Vol. 13, No. 6, 1607, 1997.
6. Zakaria, A., C. Gilmore, and J. LoVetri, "Finite-element contrast source inversion method for microwave imaging," *Inverse Problems*, Vol. 26, No. 11, 115010, 2010.
7. Rubaek, T., P. M. Meaney, P. Meincke, and K. D. Paulsen, "Nonlinear microwave imaging for breast-cancer screening using Gauss-Newton's method and the CGLS inversion algorithm," *IEEE Transactions on Antennas and Propagation*, Vol. 55, No. 8, 2320–2331, 2007.
8. Abubakar, A., T. M. Habashy, G. Pan, and M.-K. Li, "Application of the multiplicative regularized Gauss-Newton algorithm for three-dimensional microwave imaging," *IEEE Transactions on Antennas and Propagation*, Vol. 60, No. 5, 2431–2441, 2012.
9. Meaney, P. M. and K. D. Paulsen, "Theoretical premises and contemporary optimizations of microwave tomography," *Microwave Technologies*, Ch. 14, D. A. Kishk and D. K. H. Yeap, Eds., IntechOpen, Rijeka, 2022, [Online], Available: https://doi.org/10.5772/intechopen.103011.
10. Abdollahi, N., D. Kurrant, P. Mojabi, M. Omer, E. Fear, and J. LoVetri, "Incorporation of ultrasonic prior information for improving quantitative microwave imaging of breast," *IEEE Journal on Multiscale and Multiphysics Computational Techniques*, Vol. 4, 98–110, 2019.
11. Kurrant, D., A. Baran, J. LoVetri, and E. Fear, "Integrating prior information into microwave tomography Part 1: Impact of detail on image quality," *Medical Physics*, Vol. 44, No. 12, 6461–6481, 2017, [Online], Available: https://aapm.onlinelibrary.wiley.com/doi/abs/10.1002/mp.12585.
12. Kurrant, D., E. Fear, A. Baran, and J. LoVetri, "Integrating prior information into microwave tomography Part 2: Impact of errors in prior information on microwave tomography image quality," *Medical Physics (Lancaster)*, Vol. 44, No. 12, 6482–6503, 2017.
13. Ostadrahimi, M., P. Mojabi, A. Zakaria, J. LoVetri, and L. Shafai, "Enhancement of Gauss-Newton inversion method for biological tissue imaging," *IEEE Transactions on Microwave Theory and Techniques*, Vol. 61, No. 9, 3424–3434, 2013.
14. Neira, L. M., B. D. Van Veen, and S. C. Hagness, "High-resolution microwave breast imaging using a 3-D inverse scattering algorithm with a variable-strength spatial prior constraint," *IEEE Transactions on Antennas and Propagation*, Vol. 65, No. 11, 6002–6014, 2017.
15. Edwards, K., N. Geddert, K. Krakalovich, R. Kruk, M. Asefi, J. Lovetri, C. Gilmore, and I. Jeffrey, "Stored grain inventory management using neural-network-based parametric electromagnetic inversion," *IEEE Access*, Vol. 8, 207182–207192, 2020.
16. Li, L., L. Wang, F. Teixeira, L. Che, and T. Cui, "DeepNIS: Deep neural network for nonlinear electromagnetic inverse scattering," *IEEE Transactions on Antennas and Propagation*, Vol. 67, No. 3, 1819–1825, 2018.
17. Wei, Z. and X. Chen, "Deep-learning schemes for full-wave nonlinear inverse scattering problems," *IEEE Transactions on Geoscience and Remote Sensing*, Vol. 57, No. 4, 1849–1860, 2019.

18. Khoshdel, V., M. Asefi, A. Ashraf, and J. LoVetri, "Full 3D microwave breast imaging using a deep-learning technique," *Journal of Imaging*, Vol. 6, No. 8, 80, Aug. 2020, [Online], Available: http://dx.doi.org/10.3390/jimaging6080080.
19. Khoshdel, V., M. Asefi, A. Ashraf, and J. LoVetri, "A multi-branch deep convolutional fusion architecture for 3D microwave inverse scattering: Stored grain application," *Neural Computing and Applications*, 2021, [Online], Available: https://doi.org/10.1007/s00521-021-05970-3.
20. Guo, R., Z. Lin, T. Shan, X. Song, M. Li, F. Yang, S. Xu, and A. Abubakar, "Physics embedded deep neural network for solving full-wave inverse scattering problems," *IEEE Transactions on Antennas and Propagation*, Early Access Article, 1–1, 2021.
21. Zhou, Y., Y. Zhong, Z. Wei, T. Yin, and X. Chen, "An improved deep learning scheme for solving 2-D and 3-D inverse scattering problems," *IEEE Transactions on Antennas and Propagation*, Vol. 69, No. 5, 2853–2863, 2021.
22. Benny, R., T. A. Anjit, and P. Mythili, "An overview of microwave imaging for breast tumor detection," *Progress In Electromagnetics Research*, Vol. 87, 61–91, 2020.
23. Gilmore, C., M. Asefi, J. Paliwal, and J. LoVetri, "Industrial scale electromagnetic grain bin monitoring," *Computers and Electronics in Agriculture*, Vol. 136, 210–220, 2017.
24. Curlander, J. C. and R. N. McDonough, *Synthetic Aperture Radar*, Vol. 11, Wiley, New York, 1991.
25. Zhdanov, M. S., *Geophysical Inverse Theory and Regularization Problems*, Vol. 36, Elsevier, 2002.
26. Guo, R., X. Song, M. Li, F. Yang, S. Xu, and A. Abubakar, "Supervised descent learning technique for 2-D microwave imaging," *IEEE Transactions on Antennas and Propagation*, Vol. 67, No. 5, 3550–3554, 2019.
27. Chen, X., *Computational Methods for Electromagnetic Inverse Scattering*, Wiley Online Library, 2018.
28. Nemez, K., M. Asefi, A. Baran, and J. LoVetri, "A faceted magnetic field probe resonant chamber for 3D breast MWI: A synthetic study," *2016 17th International Symposium on Antenna Technology and Applied Electromagnetics (ANTEM)*, 1–3, IEEE, 2016.
29. Chen, X., Z. Wei, M. Li, and P. Rocca, "A review of deep learning approaches for inverse scattering problems (invited review)," *Progress In Electromagnetics Research*, Vol. 167, 67–81, 2020.
30. LoVetri, J., M. A. Asefi, C. Gilmore, and I. Jeffrey, "Innovations in electromagnetic imaging technology: The stored-grain-monitoring case," *IEEE Antennas and Propagation Magazine*, Vol. 62, No. 5, 33–42, 2020.
31. Li, M., R. Guo, K. Zhang, Z. Lin, F. Yang, S. Xu, X. Chen, A. Massa, and A. Abubakar, "Machine learning in electromagnetics with applications to biomedical imaging: A review," *IEEE Antennas and Propagation Magazine*, Vol. 63, No. 3, 39–51, 2021.
32. Khoshdel, V., A. Ashraf, and J. LoVetri, "Enhancement of multimodal microwave-ultrasound breast imaging using a deep-learning technique," *Sensors*, Vol. 19, No. 18, 4050, 2019.
33. Edwards, K., V. Khoshdel, M. Asefi, J. LoVetri, C. Gilmore, and I. Jeffrey, "A machine learning workflow for tumour detection in breasts using 3D microwave imaging," *Electronics*, Vol. 10, No. 6, 2021, [Online], Available: https://www.mdpi.com/2079-9292/10/6/674.
34. Reimer, T., M. Solis, and S. Pistorius, "The application of an iterative structure to the delay-and-sum and the delay-multiply-and-sum beamformers in breast microwave imaging," *Diagnostics*, Vol. 10, 411, June 2020.
35. Zakaria, A., I. Jeffrey, J. LoVetri, and A. Zakaria, "Full-vectorial parallel finite-element contrast source inversion method," *Progress In Electromagnetics Research*, Vol. 142, 463–483, 2013.
36. Geddert, N., "An electromagnetic hybridizable discontinuous Galerkin method forward solver with high-order geometry for inverse problems," 2020.